This is the accepted version of an article pubbished in Materials Science and Engineering: A, Volume 840, 18 April 2022, 142747
The final publication is available at https://dx.doi.org/10.1016/j.msea.2022.142747

# On the role of building orientation and surface post-processes on the fatigue life of Ti-6Al-4V coupons manufactured by laser powder bed fusion

Antonio Cutolo[a,b,1], Chola Elangeswaran[a,b], Gokula Krishna Muralidharan[c], Brecht Van Hooreweder[a]

[a] *KU Leuven Department of Mechanical Engineering, Celestijnenlaan 300, 3001 Leuven (Heverlee), Belgium*
[b] *SIM M3 Program, Technologiepark 48, 9052 Zwijnaarde, Belgium*
[c] *3D Systems Leuven, Grauwmeer 14, 3001, Leuven, Belgium*

## Abstract

Additive manufacturing (AM) techniques have been rapidly expanding due to their ability to produce complex geometries with an efficient material use. However one of the main drawback of AM technologies is the poor surface quality especially for what concerns powder based techniques. In order to design reliable AM parts, the material mechanical properties resulting from the manufacturing process need to be properly characterized. The present study investigates the fatigue of miniaturized Ti-6Al-4V specimens manufactured using laser powder bed fusion (L-PBF) along three different building orientations. In order to improve the surface quality, two post-treatments were applied to the test coupons, i.e. electro-plasma polishing and machining. Fatigue test results highlight how the post-treatments improve the fatigue properties of L-PBF Ti-6Al-4V samples with machined samples outperforming all the others conditions. Data gathered from the experimental campaign have been used to generate a predictive tool to account for surface quality, that can be used to foresee fatigue properties of Ti-6Al-4V samples subjected to different surface treatments.

*Keywords:* laser powder bed fusion - Ti-6Al-4V - fatigue - surface treatments

https://doi.org/10.1016/j.msea.2022.142747

## Introduction

Over the last few decades, additive manufacturing (AM) methods have grown in popularity for producing near-net-shape metallic components for a wide range of medical, aerospace, and automotive applications. One of the main advantages of AM processes over conventional manufacturing techniques is the capability to fabricate parts with efficient material use, even for customized and complex geometries [1, 2]. Moreover, the geometrical freedom guaranteed by the

*Corresponding author
*Email address:* antonio.cutolo@kuleuven.be (Antonio Cutolo)
*URL:* www.set.kuleuven.be/am/ (Antonio Cutolo)

layer-by-layer AM production is sometimes impossible to reach for conventional subtractive manufacturing techniques. Among the AM processes, laser powder bed fusion (L-PBF) can guarantee higher tolerances with better surface finish [3] when compared with electron beam powder bed fusion (EB-PBF) and direct energy deposition (DED) techniques [4].

Given their excellent properties of weldability, corrosion resistance, high strength to weight ratio, and biocompatibility, titanium alloys are very attractive for L-PBF component production. In particular, Ti-6Al-4V, when processed by L-PBF, possesses a unique microstructure and consequently unique mechanical properties that result from the peculiar L-PBF process conditions such as high localization of the energy input and the high thermal gradients [5]. However, as-manufactured parts are affected by high residual stress [6] and high surface roughness, undesired but inevitable drawbacks of the layer-by-layer production [7]. These imperfections greatly affect the parts mechanical properties, particularly when it comes to the relationship between surface quality and fatigue behaviour.

On the one hand, various researchers have emphasized the benefit of applying volumetric heat-treatments to Ti-6Al-4V parts to reduce the residual stresses [8, 9, 10] and to consequently enhance the fatigue performance [11, 12, 13]. On the other hand, significant effort has been made to improve the surface quality by reducing the surface roughness so to enhance the fatigue resistance [14, 15, 16, 17]. However, to benefit from the manufacturing capability of the L-PBF process, it is of utmost importance to understand the mechanical response of parts with as-produced surface conditions [11, 18]. In fact, surface post-treatments on complex and intricate geometries are challenging and indeed sometimes impossible to perform, and hence the as-built surface condition remains a very important condition to investigate.

In several studies, researchers have tried to define a relation between the fatigue performance of AM coupons and surface roughness, as it has been extensively shown that as-manufactured AM coupons showed crack initiation at surface roughness valleys. Thus, surface valleys can be treated as micro-notches. In this context, the focus has been concentrated either to the lowest profile valley $R_v$ as a surface parameter for fatigue analysis [19], or to a combination of surface roughness parameters [18, 20, 21], such as $R_a$, $R_v$ $R_p$. On the one hand, the use of the sole $R_v$ value only can be misleading since the stress concentration factors of notches do not depend solely on the notch depth, but rather on the notch morphology. On the other hand, the combination of several surface roughness parameters might be utilized for textured surfaces [22, 23] on which the surface morphology results mostly homogeneously all over the component. For as produced AM components, the surface morphology is highly influenced by several factors [24] such as volumetric energy density, powder particle size, building orientation etc. Each combination of these parameters could result in different as-produced surface topologies, that could degrade the mechanical properties. As an example, a recent study by du Plessis and Beretta [25] investigated the surface morphology of AlSi10Mg of as-manufactured coupons using X-ray computed tomography, revealing a large sensitivity of the process-induced micro-notches from the samples building orientation. Consequently, du Plessis and Beretta demonstrated the tremendous influence that these surface defects have on fatigue properties.

In the present study, the fatigue performance of L-PBF Ti-6Al-4V coupons has been extensively investigated to understand the relation between the surface condition and dynamic behaviour. The samples have been produced along different building directions and two different sur-

face treatments have been considered to enhance the surface quality of as-produced parts, namely electro-plasma polishing and machining. For all the investigated conditions, the surface roughness of these specimens has been comprehensively characterized through profilometry measurements. From these measurements, the valleys' local stress concentration values have been extracted together with the valleys' morphological features. The fatigue test campaign highlighted that the machining operations enhance the fatigue performance of the samples, with the coupons produced horizontally outperforming the other conditions. A limited benefit to the fatigue behaviour has also been observed for electro-plasma polished parts. However, this treatment introduced some undesired surface defects that inhibited the potential fatigue enhancement of the post-treatment.

Finally, the coupons fatigue performance has been related to critical stress concentration factors and the associated critical morphological features to generate a predictive tool to assess the fatigue properties of Ti-6Al-4V specimens.

## Materials and methods

*Production and testing*

The specimen geometry considered for the present investigation is shown in Figure 1. The geometry presents a continuous radius between the two gripping cylinders with the smallest cross-section with a diameter of $2.5mm$. This geometry has been specifically designed to assess the fatigue properties of additively manufactured metals. [11, 21, 26, 27].

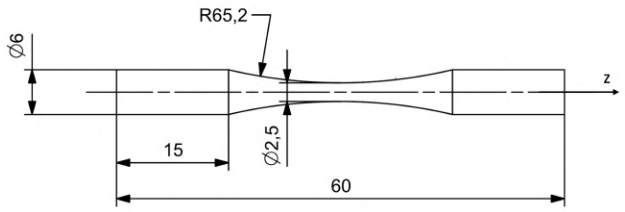


Figure 1: Fatigue test specimen geometry - dimensions in *mm*.

The test coupons were produced via the L-PBF ProX320 system (3D Systems) equipped with a $500W$ fiber-laser and a vacuum chamber to reduce the oxygen levels during production to below $50ppm$. The samples were produced using LaserForm Ti Gr23 powder (3D Systems) for Ti-6Al-4V specimens. The powder chemical composition is presented in Table 1. The parts were printed with standard LaserForm® Ti grade23 for 60µm layer thickness parameters with energy density $40J/mm^3$. LaserForm® Ti grade23 possesses a particle size distribution of $10 - 45\mu m$. Representative picture of the powder particles used for manufacturing is presented in Figure 2. Scanning strategy stripe was used. Special attention was given to avoid any oxygen pickup during manufacturing of the titanium samples by flushing the build chamber with argon and by keeping oxygen levels in the build chamber below $50ppm$.

The specimens were manufactured along three different building orientations, i.e. the sample axis ($z$ in Figure 1) was oriented with an angle of 0°, 50°, and 90° with respect to the baseplate of the L-PBF machine. To avoid severe distortions and to preserve specimen geometry, support

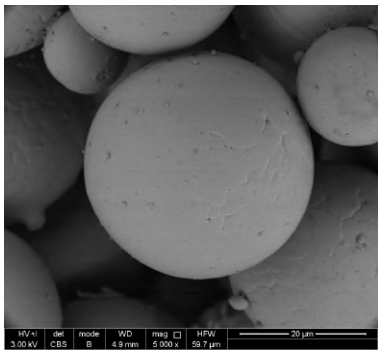

Figure 2: Scanning electron microscope picture of the LaserForm® Ti grade23 powder used for specimens manufacturing.

Table 1: LaserForm Ti Gr23 powder (3D Systems) chemical composition [28]

| Element | Ti | Al | V | Fe | O | C | H | N | Y |
|---|---|---|---|---|---|---|---|---|---|
| Weigth [%] | Bal. | 5.5 – 6.5 | 3.5 – 4.5 | < 0.25 | < 0.13 | < 0.08 | < 0.012 | < 0.03 | < 0.005 |

structures were used to produce 0° and 50° oriented samples. The 50° orientation was selected to investigate the effect of the staircase effect on up-facing and down-facing surfaces and, consequently, which of the two regions has the greater impact on fatigue performance of L-PBF Ti-6Al-4V coupons. The 0° orientation was selected to investigate the effect of down-facing un-supported surfaces. For this specific orientation, the supports were only adopted along the gripping surfaces and part of the continuous radius of the geometry. The region around the smallest cross-sections was not supported as can be observed in Figure 3.

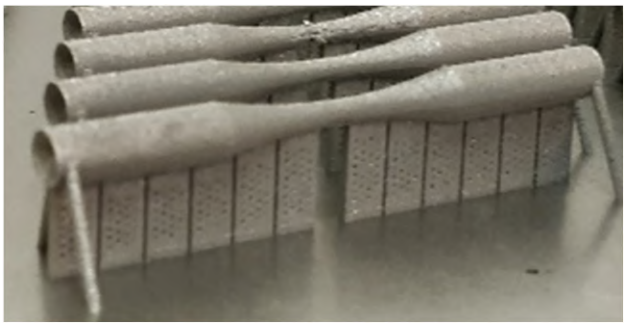

Figure 3: Support strategy for 0° oriented samples L-PBF production.

After the production, a stress-relieving (SR) operation was performed. The SR consisted of heating the specimens to a temperature of 850°C for 2 hours followed by air cooling. The use of this post-treatment was intended to eliminate any residual stress developed during the manufacturing process and to generate a fine Widmanstätten $\alpha + \beta$ microstructure [9]. Figure 4 shows an optical microscopy picture of the L-PBF Ti-6Al-4V obtained after the stress relieving operation. A Widmanstatten microstructure is depicted in this image. With a Yield strength of 914 MPa and a strain at maximum stress of 10.15% percent, this microstructure ensures an excellent compro-

mise between strength and ductility. The static characteristics of machined coupons were assessed using the ASTM E8 standard.

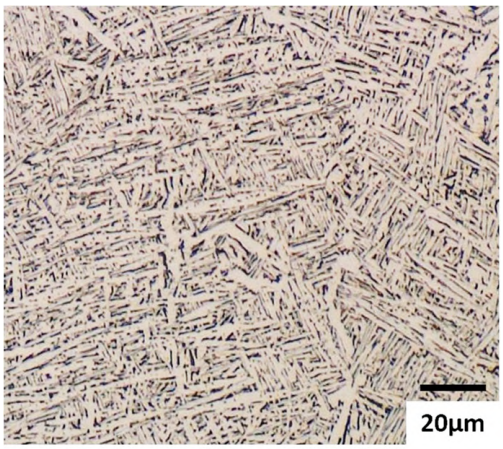


Figure 4: Ti-6Al-4V microstructure resulting from stress relieving operation.

In order to improve the surface quality of the as-produced coupons, two surface post-treatments were conducted for the three different orientations, i.e. an electro-plasma polishing (EPP) and a machining treatment (MC). EPP was performed by Plasmatec B.V. by submerging the samples in a plasma cloud, using their default parameters for titanium. After this operation, a $130\mu m$ reduction in diameter was observed. The choice of this post-treatment was based on its potential to enhance the surface quality of geometries with intricate features that would be impossible to reach with traditional turning operations. The MC samples were obtained from turning oversized hexagons to the geometry, aiming at a surface roughness smaller than $R_a < 0.2\mu m$.

A total of nine different combinations of surface and building orientation was investigated. A detailed summary of the sample conditions is presented in Table 2.

Table 2: Summary of the different investigated conditions

| Orientation | Surface condition | Batch ID |
|---|---|---|
| 0° | As-Produced | ASB - 0° |
| 50° | As-Produced | ASB - 50° |
| 90° | As-Produced | ASB - 90° |
| 0° | Electro-plasma polished | EPP - 0° |
| 50° | Electro-plasma polished | EPP - 50° |
| 90° | Electro-plasma polished | EPP - 90° |
| 0° | Machined | MC - 0° |
| 50° | Machined | MC - 50° |
| 90° | Machined | MC - 90° |

Surface roughness was measured with Mitutoyo Formtracer CS-3200S4 equipment. Three samples per condition were analysed, and three profiles per sample were measured. The measurements were performed on the external sample surface along the z direction with a resolution of

$0.5\mu m$. For 50° and 0° samples, the roughness measurements were performed on up-facing and down-facing surfaces. Special attention was adopted for 0° down-facing surface roughness. In particular, for this case, the measurement was performed along the un-supported region only, as presented in Figure 5.

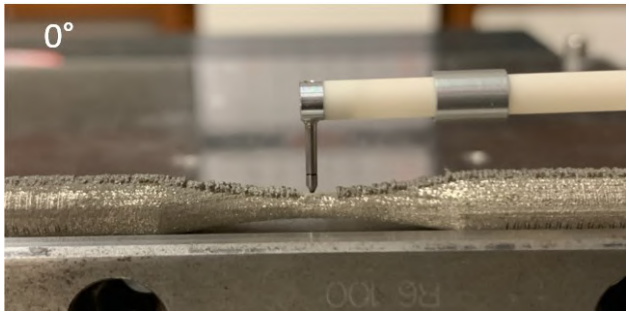


Figure 5: Representative roughness measurement operation on 0° sample down-facing surface.

Fatigue testing was performed according to ASTM E466 on an Instron E1000 machine equipped with a $10kN$ load cell. The tests were force-controlled and conducted with a constant amplitude fully reversed sinusoidal load (stress ratio $R = -1$). For each batch, at least three different stress levels were investigated and, for each stress level, at least two samples were tested. Fatigue tests were performed until the failure of the coupons or stopped if no failure occurred after $2 \cdot 10^6$ cycles.

A Philips XL 30 FEG scanning electron microscope (SEM) was used for crack initiation points identification on fractured samples.

*Surface stress concentration evaluation*

To correlate the surface condition with the fatigue behaviour of the tested samples, the stress concentration factors were extracted from the measured profiles using the approach described by Gao et al. [29, 30] and Cheng et al. [31].

According to this approach, the profiles can be treated as one side of an infinite plate subjected to the tensile stress T as indicated in Figure 6. The profiles can then be treated as a superimposition of a series of cosine components, extracted by means of spectrum analysis as in eq. 1.

$$a(x) = -\sum_{i=1}^{n} A_i cos\left(\frac{2\pi x}{\lambda_i} + \phi_i\right) \tag{1}$$

in which $a(x)$ is the measured profile, $A_i$ is the $i-th$ cosine amplitude, $\lambda_i$ is the $i-th$ cosine wavelength and $\phi_i$ is the $i-th$ cosine phase. Considering a point at depth $r$ from the surface, its

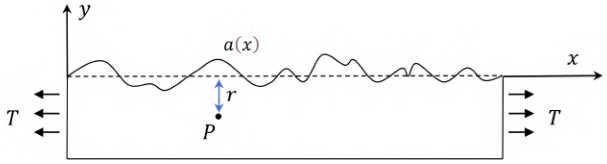


Figure 6: Infinite plate with one side presenting a wavy surface topography.

stress state is perturbed by each cosine wave and can be determined as:

$$\sigma_{xx} = T\left[1 + \sum_{i=1}^{n} \frac{4\pi A_i}{\lambda_i}\left(1 - \frac{\pi r}{\lambda_i}\right) e^{-\frac{2\pi x}{\lambda_i}} cos\left(\frac{2\pi x}{\lambda_i} + \phi_i\right)\right]$$

$$\sigma_{yy} = \sum_{i=1}^{n} \frac{4\pi^2 r A_i T}{\lambda_i^2} e^{-\frac{2\pi x}{\lambda_i}} cos\left(\frac{2\pi x}{\lambda_i} + \phi_i\right) \tag{2}$$

$$\sigma_{xy} = \sum_{i=1}^{n} \frac{2\pi A_i T}{\lambda_i^2}\left(1 - \frac{2\pi r}{\lambda_i}\right) e^{-\frac{2\pi x}{\lambda_i}} sin\left(\frac{2\pi x}{\lambda_i} + \phi_i\right)$$

From these equations, the stress concentration factor can be calculated for each point of the profile by considering $r = 0$ in the first of the eq. 2:

$$k_t(x) = \frac{\sigma_{xx}}{T} = 1 + \sum_{i=1}^{n} \frac{4\pi A_i}{\lambda_i}\left(1 - \frac{\pi r}{\lambda_i}\right) cos\left(\frac{2\pi x}{\lambda_i} + \phi_i\right) \tag{3}$$

This approach was adopted for calculating the stress concentration factors (SCF) of ASB and EPP samples for all three different building orientations. In the cases of 50° and 0°, this analysis was limited to the profiles extracted from down-facing surfaces as these regions present the worst surface roughness. For each profile, the SCF at the each valley's deepest location (defined as profile local minimum) were extracted. A generalized extreme value fitting was used to describe the SCF probability distribution for each profile. The critical notches were defined as the ones that presented a probability higher than 95%.

The critical notches were used to compute the notch sensitivity of the test specimens for different surface post-treatments and building orientations.

## Results and discussion

*Surface roughness*

The results of the surface roughness measurements performed on ASB, EPP, and MC samples are reported in Table 3.

Table 3: Surface roughness measurements for all the investigated conditions

| | | ASB | | EPP | | MC | |
|---|---|---|---|---|---|---|---|
| Orientation | Location | $R_a$ [$\mu m$] | $R_v$ [$\mu m$] | $R_a$ [$\mu m$] | $R_v$ [$\mu m$] | $R_a$ [$\mu m$] | $R_v$ [$\mu m$] |
| 90° | | 9.11 | 24.54 | 2.77 | 9.31 | | |
| 50° | Up-face | 19.38 | 57.96 | 2.49 | 7.45 | | |
| | Down-face | 23.51 | 52.03 | 7.09 | 27.40 | 0.11 | 0.40 |
| 0° | Up-face | 38.05 | 97.94 | 8.51 | 25.55 | | |
| | Down-face | 97.91 | 172.10 | 32.37 | 82.53 | | |

These measurements provide several insights. First of all, the results show how the building orientation affects the coupons surface quality on both up-facing and down-facing surfaces when compared with samples produced vertically (90°). Furthermore, 50° and 0° coupons present different surface topology for the up-facing and the down-facing areas. In the case of up-facing surfaces, the surface morphology has been generated by the pronounced stair-case effect, typical of layer-by-layer manufacturing processes of inclined surfaces. In the case of the down-facing surfaces, the morphology is altered by the dross accumulation caused by reduced heat conduction from the powder compared to solid support structures, leading to larger melt pools and hence sintering of loose powder particles to the down-facing surface. Figure 7 provides a representation of the stair-case effect for up-facing surfaces and the dross accumulation across un-supported areas for the layer-by-layer production of a dog-bone specimen along three different building directions.

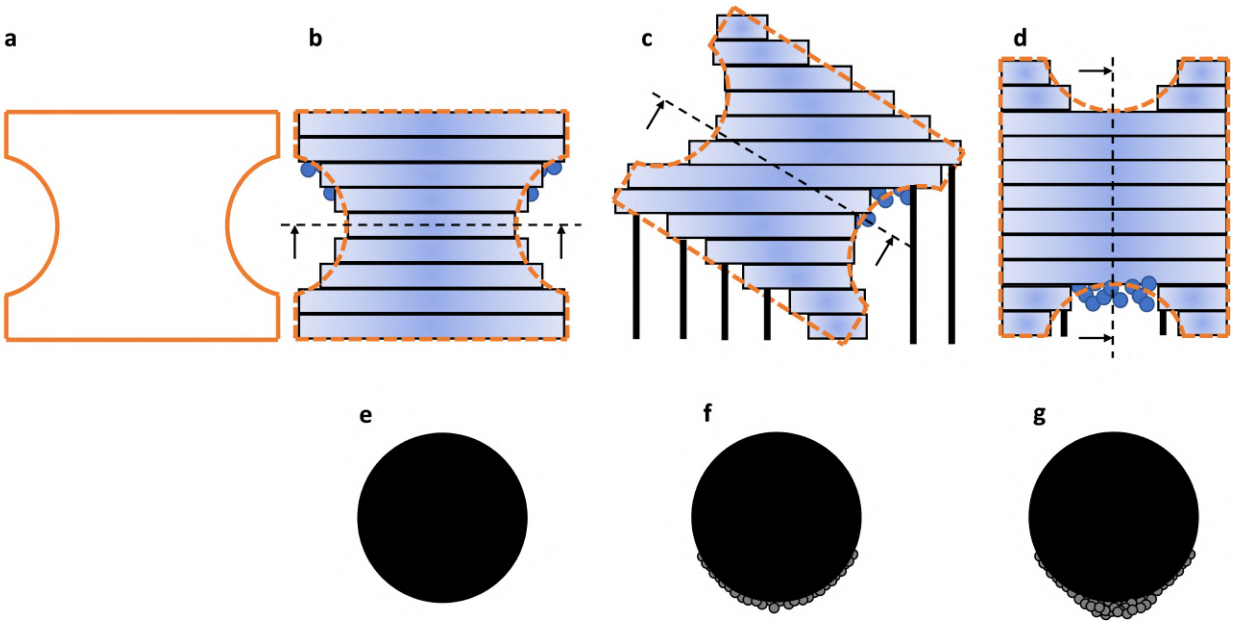


Figure 7: Schematic representation of the production of a dog-bone sample (a) by layer-by-layer powder based process. Dog bone sample produced (b) vertically, (c) with an inclination respect to the build platform, and (d) horizontally. Smallest cross-section for (e) vertical, (f) inclined, and (g) horizontal samples.

One representative as-produced sample per building orientation was cut perpendicularly to its symmetry axis ($z$ axis of Figure 1) across the smallest cross-section and inspected under an optical microscope to highlight the distortion induced by the dross formation. The results are presented in Figures 8-a, b, and c in which ASB-90°, ASB-50°, and ASB-0° cross-sections are respectively shown. As the BD inclination angle decreases from 90° to 50° and then towards 0°, the perimeter of the cross-sections presents two different types of waviness, one for the up-facing and one for the down-facing region. In the case of 50° specimens, the down-facing perimeter of Figure 8-b presents a rougher profile compared to the up-facing perimeter. This phenomena is exasperated for ASB-0° cross-section of Figure 8-c. The down-facing perimeter presents a severe waviness, and elongated dross are clearly visible. On the other hand, the up-facing perimeter also presents a rough profile resulting from the staircase effect. Although for 90° and 50° the circularity of

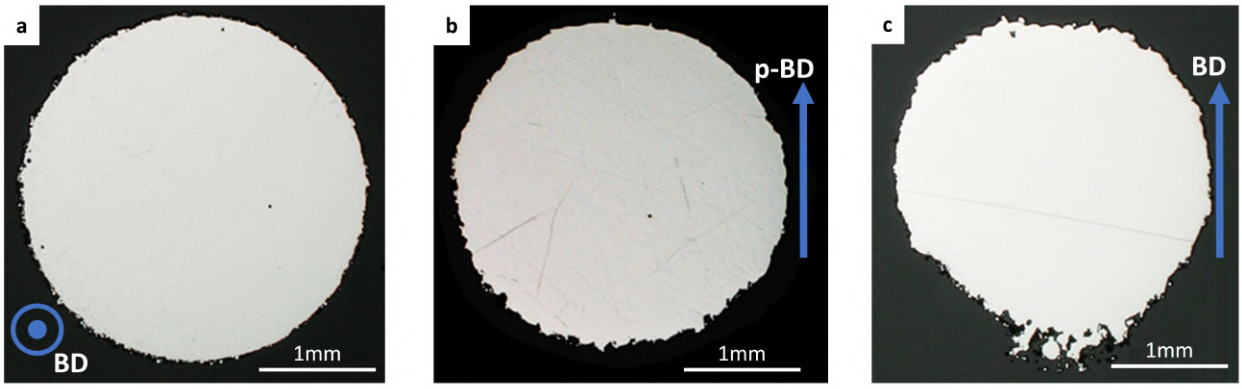


Figure 8: Cross-sections of as-produced samples for: a) 90 deg orientation; b) 50 deg orientation; c) 0 deg orientation. BD indicates the building direction and in the case of 50° samples p-BD represents the projection of the building direction on the plane of the cross section.

cross-sectional shape is preserved, for 0° the severe dross morphology distorts the cross-section circularity.

These differences in surface roughness measured on the up-facing and down-facing surfaces presented in Table 3 for as-produced specimens are direct consequence of the surface morphologies presented in Figure 8.

*Effect of surface post-treatments*

The results presented in Table 3 show how the two different post-treatments enhance the surface quality of the L-PBF test coupons.

On the one hand, the machining operations generated the best surface quality by completely removing the high waviness generated by the L-PBF process, leading to a smooth surface for the three different building orientations with a value of $R_a = 0.11\mu m$.

On the other hand, although also EPP provided a surface quality enhancement, some characteristics of the layer-by-layer production remain visible (Figure 9), especially for 50° and 0° coupons. In the case of EPP-50°, the up-facing surface is smoothed by the EPP process (Figure 9-b), whereas a relatively high waviness remains still visible on the down-facing surface (Figure 9-e). Nevertheless, the overall surface roughness was reduced for the up-facing surface from $R_a = 19.38\mu m$ of the ASB coupons to $2.49\mu m$ and for the down-facing surface from $23.51\mu m$ of the ASB coupons to $7.09\mu m$. In the case of EPP-0° samples, the surface post-treatment extensively reduced the surface roughness of the up-facing surface from $R_a = 38.05\mu m$ of the as-produced coupons to $8.51\mu m$ and for the down-facing region from $R_a = 97.91\mu m$ to $32.37\mu m$.

Nonetheless, the EPP process generated some additional defects that are clearly visible in Figure 9-d, e, and f. These defects look like craters or micro-notches randomly distributed across the external surface. This phenomenon affects the down-facing region of both EPP-50° and EPP-0° samples as indicated in Figure 9-e and f. For EPP-90°, crater-like defects are also generated (Figure 9-d). However, the density of these defects along the external surface result lower if compared with the down-facing regions of EPP-50° and EPP-0° coupons. The phenomena like the one investigated by Zangh et al. [32]. Zangh et al. showed that the EPP treatment can rip

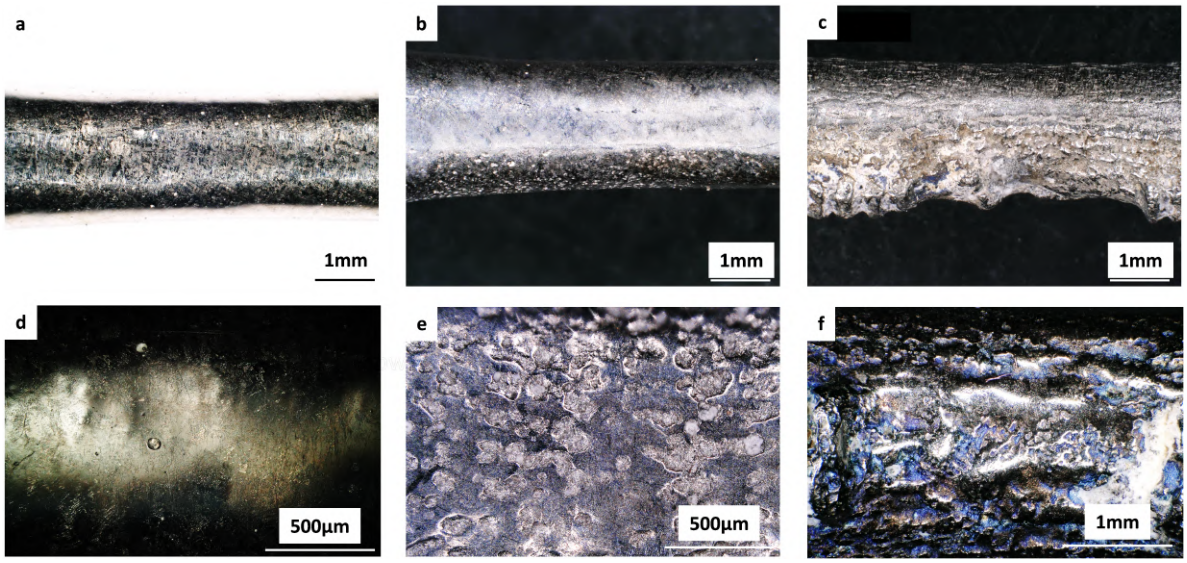


Figure 9: Surface morphology after EPP operation. a) and d) EPP 90°; b) side view of EPP 50° sample e) downfacing region for EPP 50°; c) sideview of EPP 0° sample d) downfacing region for EPP 0°.

up agglomerates of partially molten particles from the surface, leading to the generation of these craters-like defects.

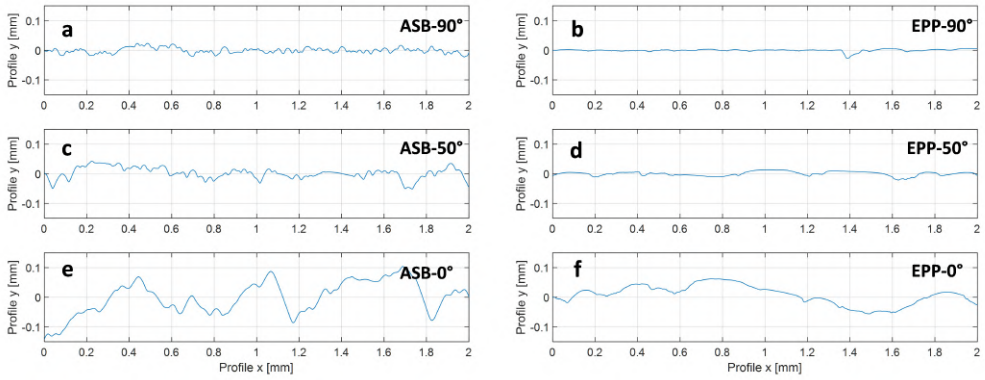


Figure 10: Representative surface profiles for: a) ASB-90°, c) ASB-50°, e), ASB-0°, b) EPP-90°, d) EPP-50° and f) EPP-0°.

Figure 10 shows representative surface profiles for as-produced and electro-plasma polished samples for the three different building orientations. Figure 10-c, d, e, and f show representative profiles of the down-facing surfaces both for 50° and 0° samples. The impact of the electro-plasma polishing on the surface of the L-PBF coupons can be clearly appreciated from the graphs of Figure 10 as the EPP process generates smoother external surfaces for all the building orientations.

*Fatigue behaviour*

Fatigue test results for all the investigated conditions are presented in Figure 11-a.

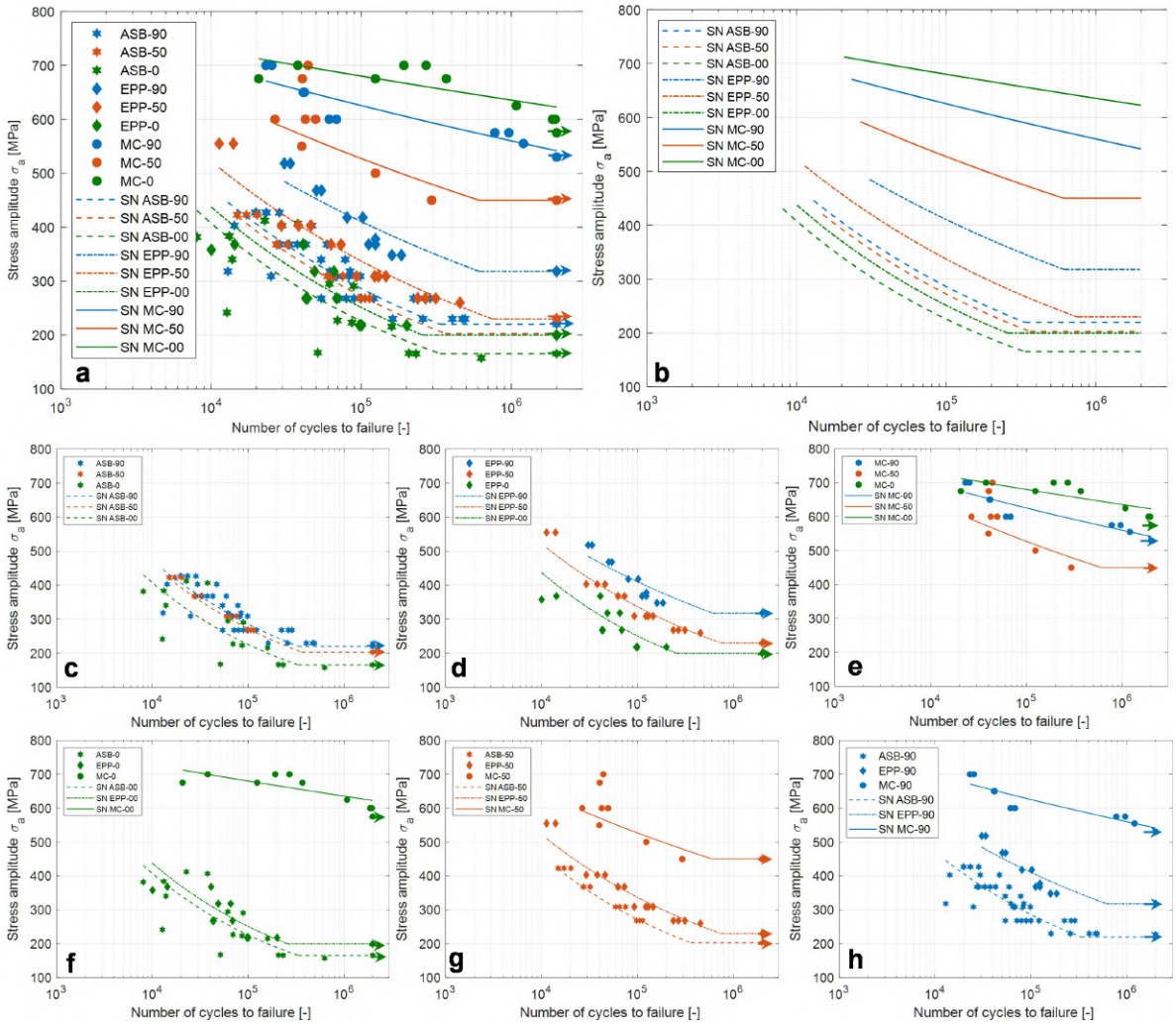


Figure 11: Fatigue test results: a) all the experimental tests; b) SN curves fitted using Basquin's equation. Experimental data and SN curves of: c) ASB specimens; d) EPP specimens; f) MC specimens in all the different building orientations. Comparison of the fatigue behaviour for different surface conditions for: f) 0° specimens; g) 50° specimens and h) 90° specimens.

The results show that the machined coupons exhibit the best fatigue performance followed by EPP and ASB samples. For EPP and ASB conditions, the 90° coupons present higher fatigue life with respect to 50° and 0° samples, with 0° showing the lowest fatigue performance in both cases Figure 11-c and Figure 11-d. Considering machined coupons, the 0° samples show higher fatigue performance with respect to the other two building orientations, with 50° samples showing the worst fatigue resistance (Figure 11-e).

For each combination of post-treatment and building orientation, the fatigue experimental data are fitted using the Basquin's equation:

$$\sigma_a = A_b(2N_f)^b \tag{4}$$

The fitting coefficients $A_b$ and $b$ are listed together with the stress amplitude of non-failed coupons in Table 4. The SN curves generated using eq. 4 are presented in Figure 11-b.

Table 4: Surface roughness measurements for all the investigated conditions

| Condition | | $A_b$ | $b$ | $\sigma_{a_{2\cdot10^6}}$ [MPa] |
|---|---|---|---|---|
| ASB | 90° | 4055 | -0.2172 | 225.5 |
| | 50° | 4402 | -0.228 | 203 |
| | 0° | 5165 | -0.2564 | 166.5 |
| EPP | 90° | 2295 | -0.141 | 330 |
| | 50° | 3424 | -0.2564 | 236.8 |
| | 0° | 4777 | -0.2413 | 200 |
| MC | 90° | 1136 | -0.0488 | 530 |
| | 50° | 3251 | -0.1474 | 450 |
| | 0° | 874.3 | -0.0295 | 575 |

The values of the run-outs obtained in the experimental were used to define the horizontal segments of the SN curves of Figure 11.

The influence of surface post-treatments may be properly appreciated by comparing the fatigue performance of coupons manufactured with the same building orientation, as shown in Figure 11-f, g and h. Regarding the samples built with 0°, the EPP treatment had a minor effect on their final fatigue life. Even though EPP improved the surface quality globally (Table 3), the high roughness of the down-facing region continue to have a negative influence on the final fatigue resistance, causing the EPP-0° coupons to performing slightly better than their as-produced counterparts, with a 20% improvement in fatigue strength at $2 \cdot 10^6$ cycles. The complete removal of the tortuous down-facing surface of 0° samples performed by the machining operation substantially improved the fatigue properties of horizontally built coupons (i.e. 0°). In this case, the fatigue strength enhancement with respect to the ASB condition is 247%.

For the 50° coupons, the EPP treatment generated an improvement of the surface quality for both un-facing and down-facing surfaces. As a result, the fatigue resistance (Figure 11-g) in the life range of $10^4 - 10^6$ cycles is considerably improved. When comparing EPP-50° and ASB-50° conditions, the fatigue strength at $2 \cdot 10^6$ cycles increased of 20%. A significant fatigue life enhancement for 50° samples has been generated by the machining operation. This post-treatment lead to a variation of the fatigue strength at $2 \cdot 10^6$ equal to 120% with respect to the ASB-50°.

The EPP process generated the highest impact on the fatigue resistance of L-PBF Ti-6Al-4V for 90° specimens (Figure 11-h), with a significant improvement of the fatigue strength of 46%. In the case of MC-90° specimens the fatigue strength enhancement is equal to 135%.

*Fractured surface*

*As built samples*

Representative fractured surfaces of as-produced samples are presented in Figure 12-a to f. All the observed coupons show similar fracture surface morphology: the fatigue failure initiate at the external surface of the coupons and propagated towards the core of the specimen until the final

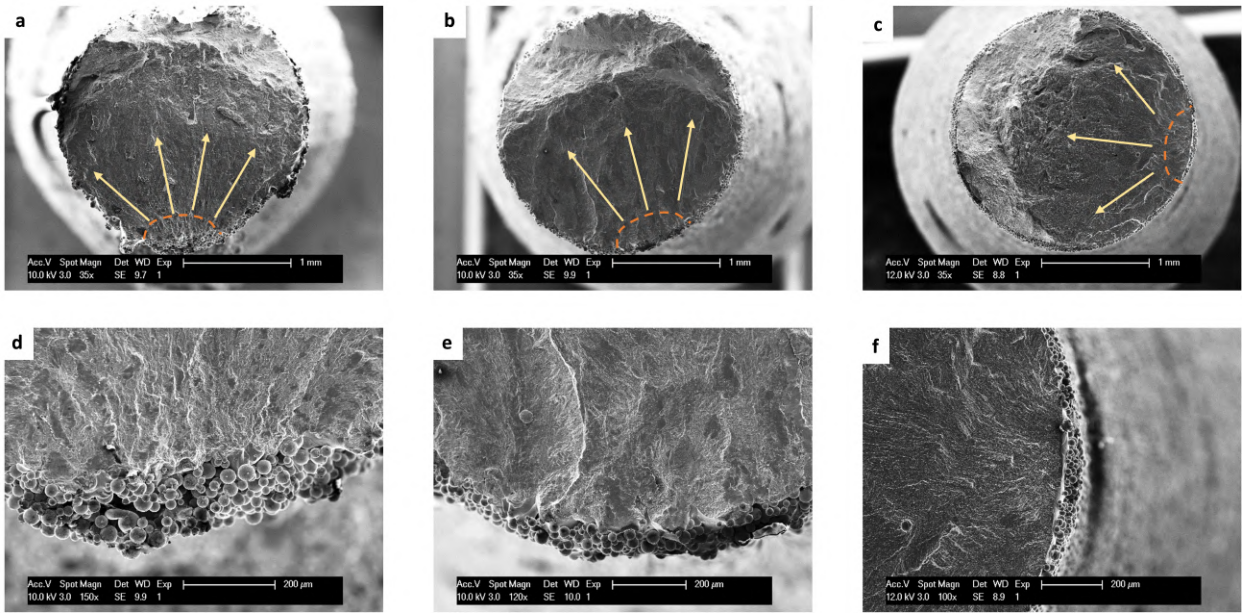


Figure 12: Fractured surfaces of ASB samples produced along a) 0°, b) 50° and c) 90° building orientation. Fatigue initiation location: d) and e) corresponds to downfacing surfaces for ASB-0° and ASB-50° respectively.

fracture. For ASB-0° the cracks were initiated at multiple locations at the down-facing surface (Figure 12-d). The initiation may be attributed to the rough morphology of the un-supported surface generated by the dross formation. The crack initiation sites correspond to valleys along the external surface that act as micro notches. The stress concentration generated at these valleys lead to crack initiation and propagation. The crack propagated from the down-facing region towards the up-facing surface (Figure 12-a).

Similar behaviour was exhibited in ASB-50° coupons. The fatigue crack initiation was observed at the un-supported down-facing surface as illustrated by Figure 12-b and e. As for ASB-0°, stress raisers across the down-facing surfaces were considered as responsible for crack initiation.

In the case of ASB-90° specimens, the crack could initiate everywhere along the specimen's external surface. The initiation sites are observed in correspondence of valleys generated by the layer by layer production.

*Electro-plasma polished samples*

Illustrative fractured surfaces of EPP samples are presented by the SEM pictures of Figure 13-a to f. Both for EPP-0° and EPP-50° specimens crack initiation occurred at the down-facing surfaces. In both cases, the EPP treatment smoothed this region, retarding the initiation and failure of the coupons. However, the down-facing region is affected by defect generated during the EPP process, that acted as local stress raisers that facilitate the crack initiation.

For EPP-90° samples similar notch-like defects initiated the damage. Even with the presence of these surface defects, the fatigue performance of 0°, 50°, and 90° samples was substantially improved by the surface treatment if compared with as-produced counterparts.

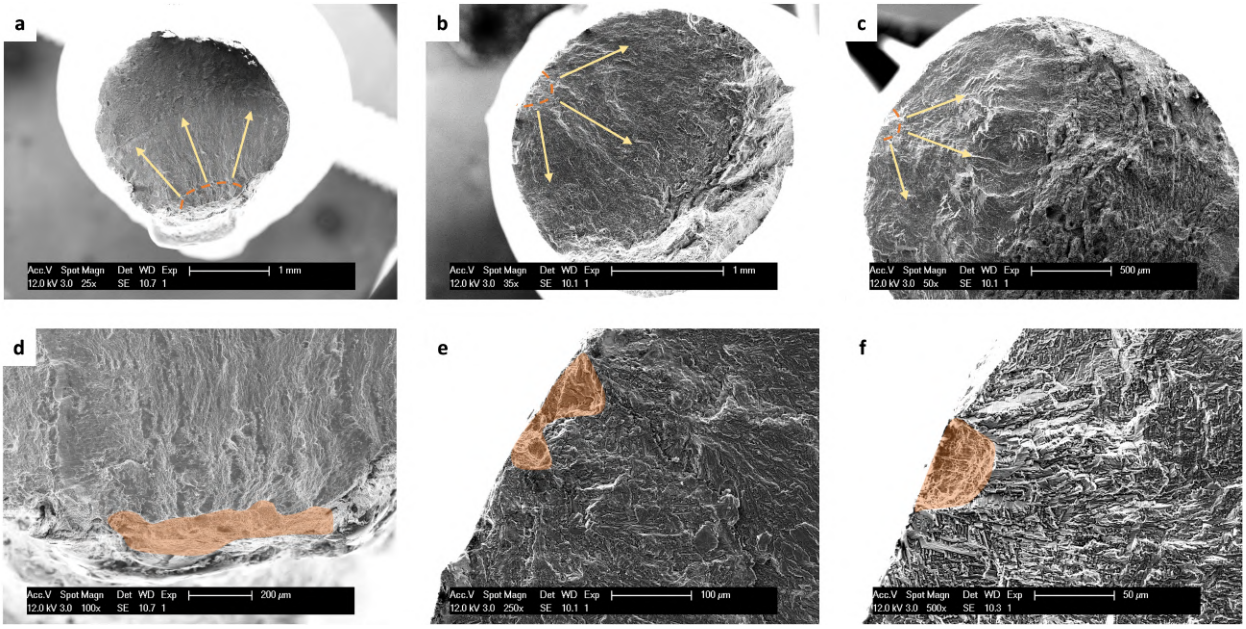


Figure 13: Fractured surfaces of EPP samples produced along a) 0°, b) 50° and c) 90° building orientation. Fatigue initiation location in d) and e) corresponds to down-facing surfaces.

*Machined samples*

Fractured surfaces of machined coupons present similar crack initiation sites for all three different building orientations. The damage initiated in proximity of spherical pores, than the crack propagated towards the center of the coupons. In the case of MC-50° and MC-90° specimens, the crack initiated at pores that were exposed to the external surface by the machining operations as indicated in Figure 14-e and f. For MC-0° samples the initiation mostly occurred from internal defects (Figure 14-d).

*Fatigue behaviour of machined coupons*

The machined coupons exhibit failure initiation either at the surface, where sub-surface pores were exposed to the external surface by the machining operation, or at internal pores that initiated the cracks. To account for such type of defects, fracture mechanics based theory has been adopted. In particular, the Murakami and Endos formula for fatigue strength evaluation in presence of sub-surface and internal pores has been used [33]. This method is based on a geometrical parameter $\sqrt{area}$ to account for the presence of defects or small cracks. $\sqrt{area}$ is the square root of the area of the defect projection on a plane perpendicular to the loading direction. The fatigue strength in presence of surface or internal defects is given by equation 5:

$$\sigma_w = \frac{F(HV + 120)}{(\sqrt{area})^{1/6}} \tag{5}$$

in which $F$ is a correction factor that accounts for the defect position (1.43 for surface defects, 1.56 for internal pores), and $HV$ is the Vickers hardness. A Vickers hardness of 383 HV was measured

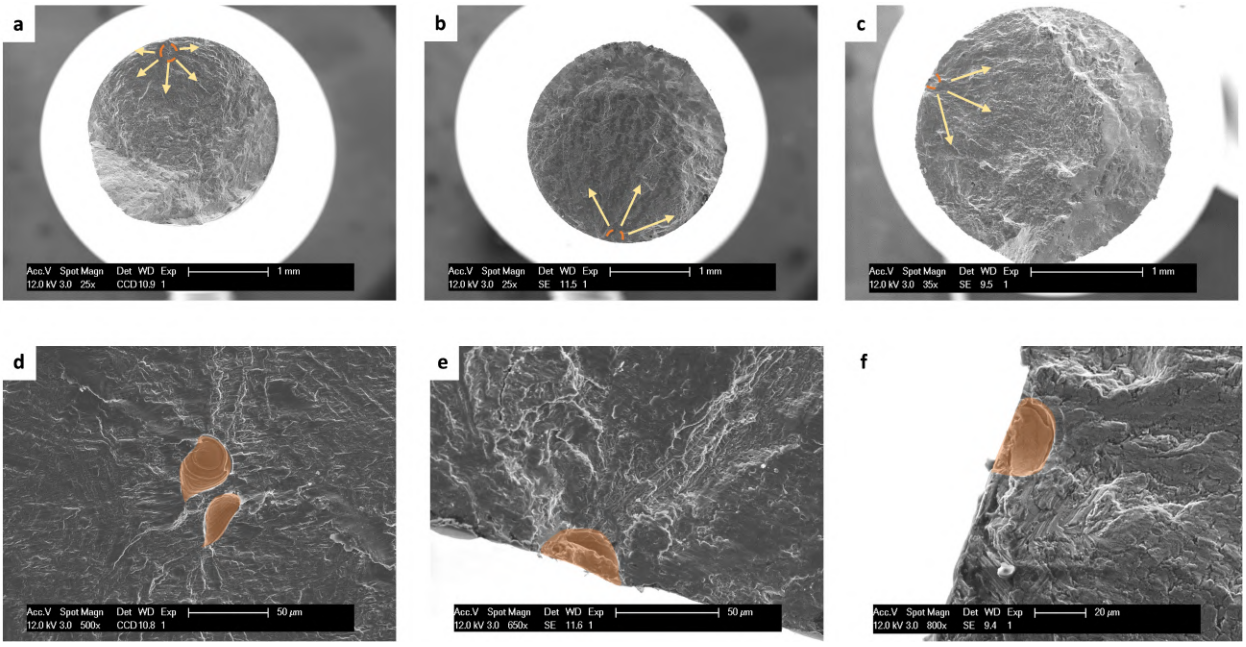


Figure 14: Fractured surfaces of MC samples produced along a) 0°, b) 50° and c) 90° building orientation.

Table 5: Defect size and fatigue strength predictions of machined coupons

| Condition | Pore *area* [$\mu m^2$] | $F$ | $\sigma_w$ [MPa] |
|---|---|---|---|
| MC-90° | 48.97 ± 18.74 | 1.43 | 521 ± 21 |
| MC-50° | 56.79 ± 25.78 | 1.43 | 515 ± 26 |
| MC-0° | 39.37 ± 15.33 | 1.56 | 578 ± 24 |

for L-PBF Ti-6Al-4V subjected to stress relieving operation.

The defect dimensions that initiated the cracks were evaluated on the SEM images of fractured surfaces via ImageJ software. The pore size (in terms of *area*) and the results of eq. 5 are reported in Table 5.

The fracture mechanics approach is able to capture the fatigue strength of the machined samples for 90° and 0° oriented samples, whereas the predictions were not as good as for 50° inclined coupons, if compared with the other two batches. In order to clarify the differences in fatigue performance showed in Figure 11 for machined coupons, a follow-up investigation is required to correlate the defect population for samples produced along different building orientations and the fatigue resistance. In fact, the sensitivity to pores of additively manufactured coupons has been extensively reported in the literature for L-PBF Ti-6Al-4V coupons produced vertically [34, 35, 36, 37, 38].

*Analysis of the surface profiles of as produced and electro-plasma polished coupons*

The data collected by surface roughness measurements have been used to calculate the critical stress concentration factors for the different surface conditions analysed. The methodology is

described in Figure 15 for one profile of an ASB-90° coupon, and it has been applied to all the other measured profiles of all the other conditions.

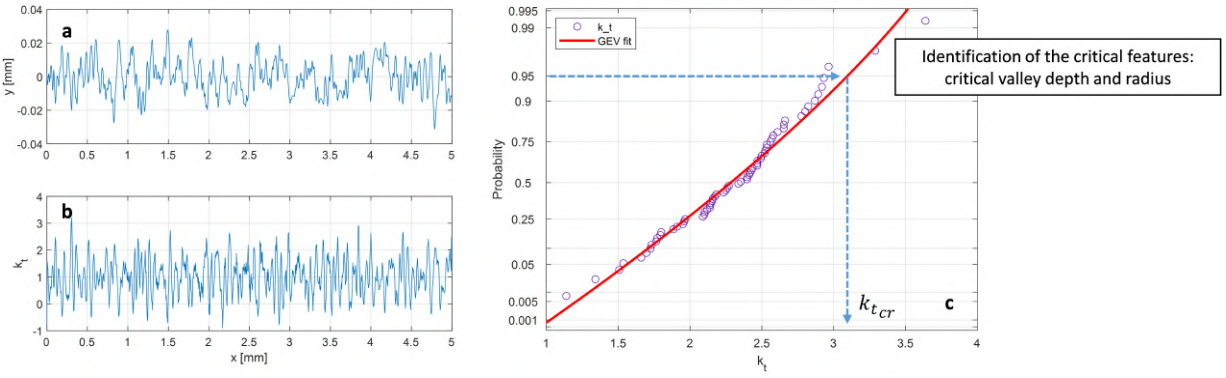


Figure 15: Extraction of the critical SCF from profile measurements.

From the profile measurements (Figure 15-a), the values of the SCF in function of the profile length, $k_t(x)$ (Figure 15-b), are evaluated using eq. 3 and the SCF at every valleys' location are extracted from $k_t(x)$. The SCF probability distributions were obtained using a generalized extreme value fitting. From these distributions, the critical notches were extracted, i.e. $k_t$ with a probability higher than 95% (Figure 15-c), and, for every critical notch, the values of notch depth and radius were stored. This process have been applied to three profiles per sample. For each condition a total of three samples have been investigated.

The average values of the $k_{t_{crit}}$, of the critical valley depths and radius are reported in Figure 16. The values of the $k_{t_{crit}}$ of Figure 16-a suggest how the different surface micro-notches generated by different building orientation and/or surface post-treatment can lead to different fatigue performance. The highest values of $k_{t_{crit}}$ for ASB-0° specimens of Figure 16-a could be considered as a clear indicator for the poor fatigue performance of these coupons.

Comparing the values of the valley depths associated with critical notches of Figure 16-b with the roughness parameter $R_v$ presented in Table 3, it emerges that they are systematically lower than the measured $R_v$ for all the surface conditions investigated, indicating that the fatigue performance has to be related to the morphology of the micro-notches rather than the sole roughness parameter $R_v$, as also indicated by other researchers [16, 20, 39].

Data shown in Figure 16 also reveal the impact of the EPP process on the critical features morphology. On the one hand, the critical valley depths exhibit a limited reduction for EPP-90° and EPP-50° if compared with their as-produced counterparts. In the case of EPP-0° specimens, the process intensively reduced the critical valley depths (Figure 16-b). On the other hand the critical notch radii become larger. These measurements indicate that the defect introduced by the EPP post-process are smooth micro-notches with blunt valley profiles (Figure 16-c).

However, the parameter that seems to better capture the trend of the stress concentration in function of the critical morphological surface features appears to be the ratio between the critical valley depth and radius (Figure 16-d). The relation between the profile morphology and the local stress concentration factors can be obtained using the relation proposed by Neuber [40]

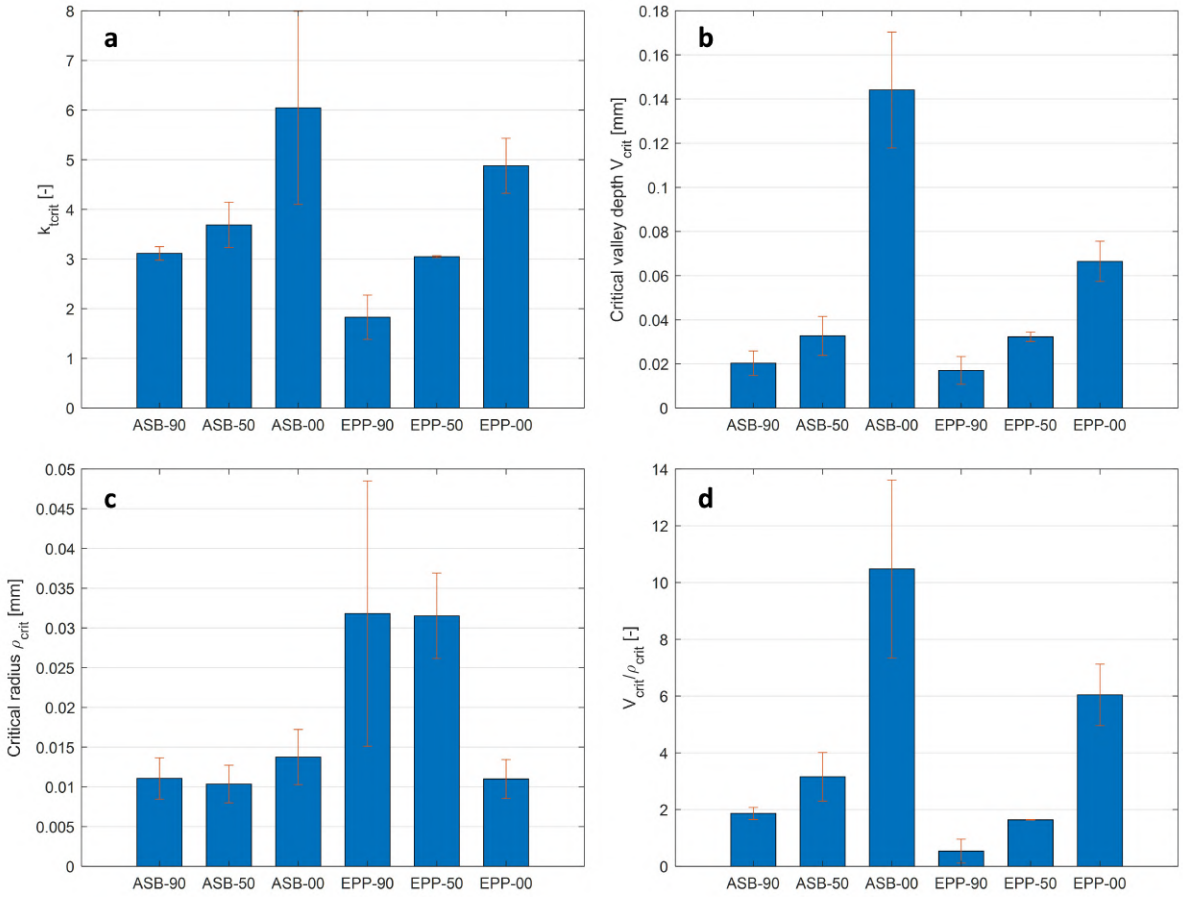


Figure 16: Profiles critical features: a) critical SCF, b) critical valley depth, c) critical radius and d) critical valley depth – radius ratio. Values expressed in terms of averages and standard deviations.

$$k_t = 1 + n\sqrt{\lambda \frac{V}{\rho}} \tag{6}$$

in which $n$ is a factor related to the type of load condition (1 for shear, 2 for tension) and $\lambda$ depends on the type of surface finishing. For the additively manufactured coupons used in this investigation, eq. 6 properly captures the dependency of the SCF from the micro-notches characteristics. The $\lambda$ coefficient has been found to be equal to 0.66 by curve fitting.

*Notch sensitivity*

The values of the critical SCF have been adopted to evaluate the notch sensitivity factor for each condition via the following expression:

$$q = \frac{k_f - 1}{k_{t_{crit}} - 1} \tag{7}$$

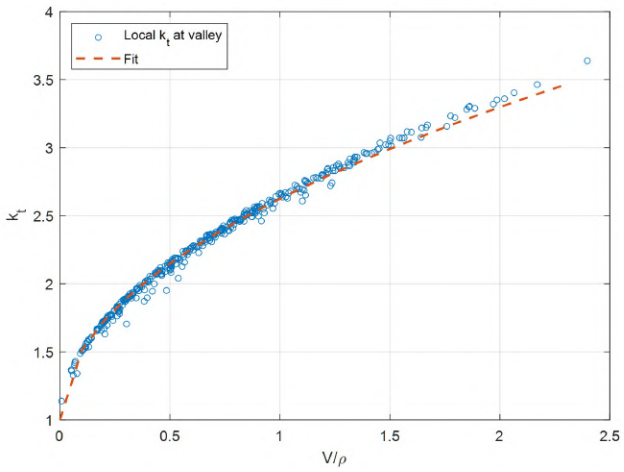


Figure 17: Stress concentration factors in function of the valley to radius ratio for one profile extracted from a ASB-90° coupon.

Table 6: Notch sensitivity factors $q$ calculated for ASB and EPP coupons

| Condition | Orientation | $q$ |
|---|---|---|
| ASB | 90° | 0.71 |
| | 50° | 0.68 |
| | 0° | 0.49 |
| EPP | 90° | 0.79 |
| | 50° | 0.71 |
| | 0° | 0.48 |

in which $k_f$ is the fatigue notch factor defined as the ratio of the run-out stress amplitude for plain coupons and the run-out stress amplitude for notched ones. For the present investigation, the run-out stress amplitude of plain specimens has been considered the run-out stress for MC-0° specimens expressed in Table 4.

In general, the notch sensitivity factor $q$ varies between 0 and 1. Low $q$ values indicate a low material notch sensitivity, namely the fatigue properties of notched samples are similar to un-notched coupons. High $q$ values indicate high material notch sensitivity with large differences between the fatigue properties of the un-notched and notched coupons.

Results of eq. 7 reported in Table 6 denote different sensitivities for different conditions. It emerges that a larger the notch factor correspond to a lower notch sensitivity. This behaviour could be explained by the relation between the notch sensitivity, stress gradient, and microstructural features expressed by Peterson [41] and re-adapted to L-PBF Ti-6Al-4V by the authors of the present investigation in an article under revision on the Fatigue & Fracture of Engineering Materials & Structures journal (FFEMS) - preprint available [42]. Specimens that exhibited larger stress drop across one single grain are less notch sensitive. Larger stress drop across one grain can be obtained either by higher SCF or by larger grain size. In the case of the present study, all the specimens possess the same microstructure, as they all underwent the same stress-relieving

operation. Therefore, the drop in the notch sensitivity factor for horizontally produced coupons can be attributed to the high notch SCF of their down-facing surfaces, both for as-produced and electro-plasma polished coupons.

*Relation between SN curves and critical morphological features*

The coefficients of the Basquin's equation $A_b$ and $b$ are usually material constants that can been obtained by curve fitting, indicating the y-intercept and the negative slope of an SN curve. In the present study, these coefficients are strongly related to the surface roughness of the tested coupons. On the one hand, $A_b$ increases with the increasing surface roughness, whereas, on the other hand, low values of the surface roughness led to small negative slope $b$ of the SN curve.

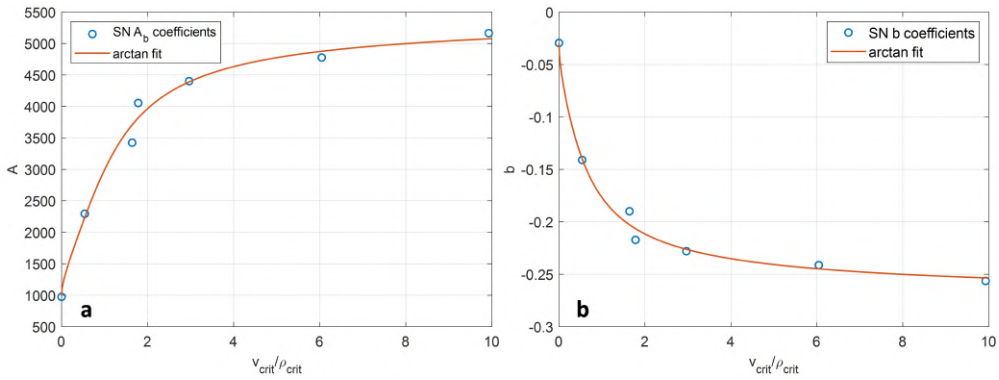


Figure 18: Basquin's equation coefficients in function of the critical valley depth to radius ratio.

In general, if $A_b$ and $b$ are known, the fatigue resistance of a material can be predicted. To evaluate the Basquin's equation coefficients for L-PBF Ti-6Al-4V in function of the surface condition, two empirical functions relating $A_b$ and $b$ with the ratio between the critical valley depth and radius (eq. 8a and eq. 8b) were extracted from Figure 18-a and b. By substituting these relations in eq. 4, the Basquin's relation can been reformulated as presented by eq. 8c.

$$A_b(k_t) = A_b\left(\frac{V_{crit}}{\rho_{crit}}\right) = 1791 atan\left(1 + 2\sqrt{0.66\frac{V_{crit}}{\rho_{crit}} - 2.5}\right) + 2742, \tag{8a}$$

$$b(k_t) = b\left(\frac{V_{crit}}{\rho_{crit}}\right) = -0.1083\left[atan\left(1 + 2\sqrt{0.66\frac{V_{crit}}{\rho_{crit}} - 1.9}\right) - 1\right], \tag{8b}$$

$$\sigma_a\left(N_f, \frac{V_{crit}}{\rho_{crit}}\right) = A_b\left(\frac{V_{crit}}{\rho_{crit}}\right)(2N_f)^{b\left(\frac{V_{crit}}{\rho_{crit}}\right)}, \tag{8c}$$

The relation expressed by eq. 8c depicts an $SN - \dfrac{V_{crit}}{\rho_{crit}}$ surface that provides for the fatigue resistance of L-PBF Ti-6Al-4V in function of the critical morphological features of the surface. Figure 19 shows the comparison between the $SN - \dfrac{V_{crit}}{\rho_{crit}}$ surface and the fitted SN curves of ASB and EPP coupons for all the different building orientations, showed in Figure 11-b. From this

comparison, it emerges that the $SN - \frac{V_{crit}}{\rho_{crit}}$ surface captures the fatigue properties of the material for a wide range of surface roughness very well and thus it could be used as a predictive tool to estimate the L-PBF Ti-6Al-4V fatigue resistance subjected to different surface treatments leading to a sensible reduction of the number of specimens to be experimentally tested.

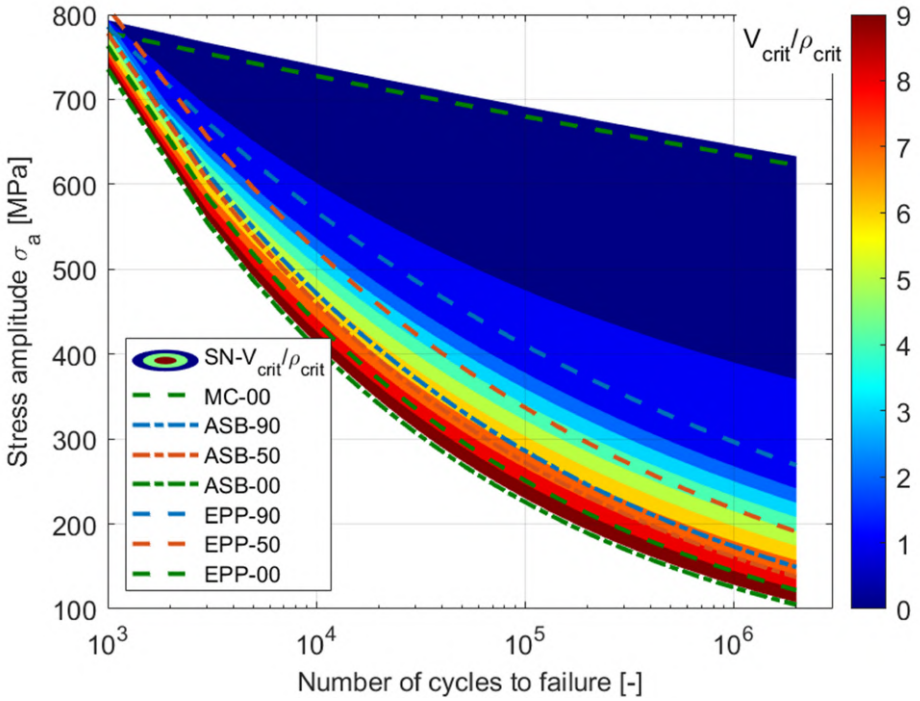


Figure 19: $SN - \frac{V_{crit}}{\rho_{crit}}$ surface compared to the EPP and ASB SN curves.

A methodology to evaluate the stress concentration across as-produced surfaces of Ti-6Al-4V coupons and consequently the fatigue resistance of the material, has been recently proposed by Lee et al. [43]. In that study the fatigue resistance of the coupons has been related to global surface roughness parameters. Lee et al. also pointed out that using $R_v$ as the main parameter to predict fatigue lives of as-produced coupons could lead to wrong evaluations. Therefore Lee et al. proposed that the surface parameters representing the height data distribution such as mode, skewness and kurtosis need to be considered together with the maximum valley depth value. Considering this hybrid surface roughness parameter together with material properties, Lee et al. were able to develop a fatigue life prediction tool. Even though this tool has great prediction capabilities, it still relies on global surface roughness and in some conditions could lead to overestimations of the fatigue performance. As a matter of fact considering EPP-90° the hybrid surface roughness parameter might not account for the micro-notches generated by the electro-plasma polishing operations. Results of the SCF evaluation using Lee et al. approach yield to a $k_t = 1.31$ which indeed underestimates the fatigue properties of the EPP-90° coupons. This further indicates the strength and applicability of the method developed in this paper.

## Conclusions

The main results and insights of the investigation conducted on L-PBF Ti-6Al-4V coupons produced with different orientations and processed with electro-plasma polishing and machining can be summarized as follows:

- Fatigue performance of as-produced L-PBF Ti-6Al-4V test coupons are mostly influenced by the surface condition which in turn is influenced by the sample's building orientation with vertically built samples overperforming the 50° and 0° ones.
- Electro-plasma polishing operations can enhance the coupons fatigue properties for the three building orientations. For EPP samples, 90° oriented samples exhibit better performance followed by 50° and 0°. Unfortunately, this post-process introduced some additional defects that reduced the fatigue enhancement capabilities of the EPP. A fine-tuning of the EPP parameters could lead to superior fatigue life than the one shown in this investigation.
- Machining post-process yield the highest fatigue performance by completely removing the typical L-PBF induced surface waviness. In this case, 0° specimens outperformed 90° and 50° ones. For MC coupons the failure mechanism is driven by surface and sub-surface pores.
- A methodology for evaluating the surface stress concentration factors based on surface roughness profile measurements was proposed. Results indicated that the most influential surface parameter is the valley depth to radius ratio indicating that the geometry of surface defects plays the most important role on fatigue performance rather than considering the deepest valley depth alone. Critical valley depth to radius has been related to the SCF by using a formulation proposed by Neuber and adapted to additively manufactured surfaces.
- A $SN - \frac{V_{crit}}{\rho_{crit}}$ surface has been evaluated that correlates fatigue performance with the surface critical morphological features. This surface can be used as a fatigue predictive tool for Ti-6Al-4V coupons treated with different surface finishing techniques.

## Data availability

The data that support the findings of this study are available from the corresponding author Antonio Cutolo.

## Authors' contribution

**Antonio Cutolo:** Conceptualization, Investigation, Methodology, Data curation, Formal analysis, Writing original draft. **Chola Elangeswaran:** Investigation, Formal analysis, Writing- Reviewing and Editing. **Gokula Krishna Muralidharan:** Resources. **Brecht Van Hooreweder:** Funding acquisition, Supervision, Project administration, Writing- Reviewing and Editing,

## Acknowledgement

The authors would like to acknowledge the financial support of SIM (Strategic Initiative Materials in Flanders) and VLAIO (Flemish government agency, Flanders Innovation & Entrepreneurship) through the M3-FATAM project (*HBC*.2016.0446), part of the MacroModelMat (M3) research program, coordinated by Siemens (Siemens Digital Industries Software, Belgium). Moreover, the authors thankfully acknowledge 3D-Systems Leuven for the high quality of the parts that were provided to conduct this investigation.

## References

[1] J. O. Milewski, Additive manufacturing of metals, Cham: Springer International Publishing (2017).

[2] D. Herzog, V. Seyda, E. Wycisk, C. Emmelmann, Additive manufacturing of metals, Acta Materialia 117 (2016) 371–392.

[3] G. N. Levy, R. Schindel, J. P. Kruth, RAPID MANUFACTURING AND RAPID TOOLING WITH LAYER MANUFACTURING (LM) TECHNOLOGIES, STATE OF THE ART AND FUTURE PERSPECTIVES 52 (2) 589–609. doi:10.1016/S0007-8506(07)60206-6.

[4] T. DebRoy, H. L. Wei, J. S. Zuback, T. Mukherjee, J. W. Elmer, J. O. Milewski, A. M. Beese, A. Wilson-Heid, A. De, W. Zhang, Additive manufacturing of metallic components – process, structure and properties 92 112–224. doi:10.1016/j.pmatsci.2017.10.001.

[5] L. Thijs, F. Verhaeghe, T. Craeghs, J. V. Humbeeck, J.-P. Kruth, A study of the microstructural evolution during selective laser melting of Ti–6Al–4V 58 (9) 3303–3312. doi:10.1016/j.actamat.2010.02.004.

[6] Z. Xiao, C. Chen, H. Zhu, Z. Hu, B. Nagarajan, L. Guo, X. Zeng, Study of residual stress in selective laser melting of Ti-6Al-4V 193 108846. doi:10.1016/j.matdes.2020.108846.

[7] P. Mercelis, J. Kruth, Residual stresses in selective laser sintering and selective laser melting 12 (5) 254–265, publisher: Emerald Group Publishing Limited. doi:10.1108/13552540610707013.

[8] B. Vrancken, R. Wauthlé, J.-P. Kruth, J. Van Humbeeck, Study of the influence of material properties on residual stress in selective laser melting, 2013, pp. 393–407.

[9] B. Vrancken, L. Thijs, J.-P. Kruth, J. Van Humbeeck, Heat treatment of Ti-6Al-4V produced by Selective Laser Melting: Microstructure and mechanical properties 541 177–185. doi:10.1016/j.jallcom.2012.07.022.

[10] Ó. Teixeira, F. J. Silva, L. P. Ferreira, E. Atzeni, A review of heat treatments on improving the quality and residual stresses of the Ti-6Al-4V parts produced by additive manufacturing, Metals 10 (8) (2020) 1006.

[11] A. Cutolo, C. Elangeswaran, C. de Formanoir, G. K. Muralidharan, B. Van Hooreweder, Effect of heat treatments on fatigue properties of Ti–6Al–4V and 316L produced by laser powder bed fusion in as-built surface condition, in: TMS 2019 148th Annual Meeting & Exhibition Supplemental Proceedings, The Minerals, Metals & Materials Series, Springer International Publishing, pp. 395–405.

[12] M. Frkan, R. Konecna, G. Nicoletto, L. Kunz, Microstructure and fatigue performance of SLM-fabricated Ti-6Al-4V alloy after different stress-relief heat treatments, Transportation Research Procedia 40 (2019) 24–29.

[13] A. K. Syed, B. Ahmad, H. Guo, T. Machry, D. Eatock, J. Meyer, M. E. Fitzpatrick, X. Zhang, An experimental study of residual stress and direction-dependence of fatigue crack growth behaviour in as-built and stress-relieved selective-laser-melted Ti-6Al-4V, Materials Science and Engineering: A 755 (2019) 246–257.

[14] L. Denti, E. Bassoli, A. Gatto, E. Santecchia, P. Mengucci, Fatigue life and microstructure of additive manufactured Ti-6Al-4V after different finishing processes, Materials Science and Engineering: A 755 (2019) 1–9.

[15] N. N. Kumbhar, A. Mulay, Post processing methods used to improve surface finish of products which are manufactured by additive manufacturing technologies: a review, Journal of The Institution of Engineers (India): Series C 99 (4) (2018) 481–487.

[16] S. Lee, Z. Ahmadi, J. W. Pegues, M. Mahjouri-Samani, N. Shamsaei, Laser polishing for improving fatigue performance of additive manufactured Ti-6Al-4V parts, Optics & Laser Technology 134 (2021) 106639.

[17] L. Hackel, J. R. Rankin, A. Rubenchik, W. E. King, M. Matthews, Laser peening: A tool for additive manufacturing post-processing, Additive Manufacturing 24 (2018) 67–75.

[18] J. Pegues, M. Roach, R. S. Williamson, N. Shamsaei, Surface roughness effects on the fatigue strength of additively manufactured Ti-6Al-4V, International Journal of Fatigue 116 (2018) 543–552.
[19] J. Gockel, L. Sheridan, B. Koerper, B. Whip, The influence of additive manufacturing processing parameters on surface roughness and fatigue life, International Journal of Fatigue 124 (2019) 380–388.
[20] J. W. Pegues, N. Shamsaei, M. D. Roach, R. S. Williamson, Fatigue life estimation of additive manufactured parts in the as-built surface condition, Material Design & Processing Communications 1 (3) (2019) e36.
[21] C. Elangeswaran, K. Gurung, R. Koch, A. Cutolo, B. V. Hooreweder, Post-treatment selection for tailored fatigue performance of 18Ni300 maraging steel manufactured by laser powder bed fusion 43 (10) 2359–2375, _eprint: https://onlinelibrary.wiley.com/doi/pdf/10.1111/ffe.13304. doi:https://doi.org/10.1111/ffe.13304.
[22] D. Arola, M. Ramulu, An examination of the effects from surface texture on the strength of fiber reinforced plastics, Journal of Composite Materials 33 (2) (1999) 102–123.
[23] D. Novovic, R. Dewes, D. Aspinwall, W. Voice, P. Bowen, The effect of machined topography and integrity on fatigue life, International Journal of Machine Tools and Manufacture 44 (2-3) (2004) 125–134.
[24] A. Charles, A. Elkaseer, U. Paggi, L. Thijs, V. Hagenmeyer, S. Scholz, Down-facing surfaces in laser powder bed fusion of Ti-6Al-4V: Effect of dross formation on dimensional accuracy and surface texture 102148doi:10.1016/j.addma.2021.102148.
[25] A. Du Plessis, S. Beretta, Killer notches: the effect of as-built surface roughness on fatigue failure in Al-Si-10Mg produced by laser powder bed fusion, Additive Manufacturing 35 (2020) 101424.
[26] C. Elangeswaran, A. Cutolo, G. K. Muralidharan, C. de Formanoir, F. Berto, K. Vanmeensel, B. Van Hooreweder, Effect of post-treatments on the fatigue behaviour of 316L stainless steel manufactured by laser powder bed fusion 123 31–39. doi:10.1016/j.ijfatigue.2019.01.013.
[27] C. Elangeswaran, A. Cutolo, G. K. Muralidharan, K. Vanmeensel, B. Van Hooreweder, Microstructural analysis and fatigue crack initiation modelling of additively manufactured 316L after different heat treatments 194 108962. doi:10.1016/j.matdes.2020.108962.
[28] Tech specs | 3d systems.
URL https://www.3dsystems.com/materials/laserform-ti-gr-23/tech-specs
[29] H. Gao, Stress concentration at slightly undulating surfaces 39 (4) 443–458. doi:10.1016/0022-5096(91)90035-M.
[30] H. Gao, A boundary perturbation analysis for elastic inclusions and interfaces 28 (6) 703–725. doi:10.1016/0020-7683(91)90151-5.
[31] Z. Cheng, R. Liao, W. Lu, Surface stress concentration factor via fourier representation and its application for machined surfaces 113-114 108–117. doi:10.1016/j.ijsolstr.2017.01.023.
[32] Y. Zhang, Electropolishing mechanism of Ti-6Al-4V alloy fabricated by selective laser melting 4792–4807doi:10.20964/2018.05.79.
[33] Y. Murakami, Metal fatigue: effects of small defects and nonmetallic inclusions, Academic Press, 2019.
[34] M. Benedetti, V. Fontanari, M. Bandini, F. Zanini, S. Carmignato, Low- and high-cycle fatigue resistance of Ti-6Al-4V ELI additively manufactured via selective laser melting: Mean stress and defect sensitivity 107 96–109. doi:10.1016/j.ijfatigue.2017.10.021.
[35] E. Wycisk, S. Siddique, D. Herzog, F. Walther, C. Emmelmann, Fatigue performance of laser additive manufactured Ti–6Al–4V in very high cycle fatigue regime up to 109 cycles 2. doi:10.3389/fmats.2015.00072.
[36] E. Wycisk, S. Siddique, D. Herzog, F. Walther, C. Emmelmann, Fatigue performance of laser additive manufactured Ti–6Al–4V in very high cycle fatigue regime up to 109 cycles 2. doi:10.3389/fmats.2015.00072.
[37] A. Fatemi, R. Molaei, J. Simsiriwong, N. Sanaei, J. Pegues, B. Torries, N. Phan, N. Shamsaei, Fatigue behaviour of additive manufactured materials: An overview of some recent experimental studies on Ti-6Al-4V considering various processing and loading direction effects 42 (5) 991–1009, _eprint: https://onlinelibrary.wiley.com/doi/pdf/10.1111/ffe.13000. doi:https://doi.org/10.1111/ffe.13000.
[38] P. Li, D. H. Warner, A. Fatemi, N. Phan, Critical assessment of the fatigue performance of additively manufactured Ti–6Al–4V and perspective for future research 85 130–143. doi:10.1016/j.ijfatigue.2015.12.003.
[39] T. D. Dinh, S. Han, V. Yaghoubi, H. Xiang, H. Erdelyi, T. Craeghs, J. Segers, W. Van Paepegem, Modeling detrimental effects of high surface roughness on the fatigue behavior of additively manufactured Ti-6Al-4V

alloys 144 106034. doi:10.1016/j.ijfatigue.2020.106034.
[40] H. Neuber, Theory of Notch Stresses: Principles for Exact Stress Calculation, J. W. Edwards, google-Books-ID: y2c0AAAAMAAJ.
[41] R. E. Peterson, Methods of correlating data from fatigue tests of stress concentration specimens 179Publisher: Macmillan New York.
[42] A. Cutolo, C. Elangeswaran, G. K. Muralidharan, B. V. Hooreweder, On the fatigue notch sensitivity of Ti-6Al-4V specimens with $\alpha$+$\beta$ microstructure produced by laser powder bed fusion. doi:10.22541/au.162092193.35740556/v1.
[43] S. Lee, B. Rasoolian, D. F. Silva, J. W. Pegues, N. Shamsaei, Surface roughness parameter and modeling for fatigue behavior of additive manufactured parts: A non-destructive data-driven approach 46 102094.